Catalysis Science & Technology

PAPER

Cite this: *Catal. Sci. Technol.*, 2016, **6**, 3976

Alkaline-assisted Ni nanocatalysts with largely enhanced low-temperature activity toward CO_2 methanation†

Jie Liu,[a] Weihan Bing,[a] Xiaoge Xue,[a] Fei Wang,[a] Bin Wang,[b] Shan He,*[a] Yingkui Zhang[a] and Min Wei*[a]

Received 25th November 2015,
Accepted 13th January 2016

DOI: 10.1039/c5cy02026c

www.rsc.org/catalysis

The CO_2 methanation reaction is a promising approach for the chemical transformation of carbon dioxide into useful fuels or products. The key challenge at present relies on the design and exploration of non-noble metal catalysts so as to achieve high activity at a low reaction temperature. In this work, we have obtained alkaline-assisted Ni nanocatalysts supported on Mg/Al mixed metal oxides (denoted as Ni_x/Mg_{2-x}Al-MMO) derived from Ni-Mg-Al hydrotalcite precursors. The catalytic performance toward CO_2 methanation was studied in detail, and the best low-temperature reaction activity was obtained over Ni/MgAl-MMO (CO_2 conversion: 97.9%; selectivity: 97.5%; 250 °C). By establishing the correlation between the catalytic performance and the alkaline site structure, it is found that the Ni nanoparticles and MgO base sites at the interface serve as dual active centers to cooperatively catalyze CO_2 methanation, resulting in low-temperature reaction activity. Moreover, *in situ* diffuse reflectance Fourier transform infrared spectroscopy (*in situ* DRIFTS) demonstrates that MgO acts as the active site for CO_2 activation to give carbonate/hydrocarbonate species, while Ni provides H-species for further hydrogenation of intermediates. Therefore, this work rationalizes the significant influence of alkaline-assisted Ni nanoparticles on CO_2 methanation, which provides a promising heterogeneous catalyst for this reaction.

1. Introduction

The chemical transformation of CO_2 from industrial exhaust gas (*e.g.*, H_2-rich coke oven gas,[1] COG) into value-added chemical fuels is of vital importance for promoting energy regeneration and solving environmental problems.[2] The hydrogenation of CO_2 to methane is one of the most promising CO_2 conversion processes.[3] Currently, studies on CO_2 methanation have been focused on the design of supported non-noble catalysts with enhanced low-temperature activity and stability.[4] It has been widely accepted that introduction of alkaline species onto a support is an effective way to increase catalytic activity and stability.[5] Previous investigations mainly involve changing the category and quantity of alkali species in a support so as to obtain enhanced catalytic activity. As is well known, the catalytic performance of alkaline is substantially determined by its structure/property on a surface (*e.g.*, type, strength, concentration, dispersion and stability).[6] Park *et al.* proposed that an alkaline site can initiate the methanation reaction by binding a CO_2 molecule to form a carbonate species, followed by hydrogenation with dissociated hydrogen to produce methane, based on DFT calculations.[7] However, experimental evidence concerning the influence of alkaline site structures on catalytic performance is rather lacking, and how to create desirable alkaline sites remains a challenge. Therefore, a systematic research on an alkaline site structure and its catalytic mechanism would be valuable for the rational design of new catalysts with largely improved catalytic performance.

Layered double hydroxides[8] (LDHs) are a class of two-dimensional (2D) anionic clays consisting of positively charged host layers and exchangeable interlayer anions, which can be generally expressed by the formula $[M^{2+}_{1-x}M^{3+}_{x}(OH)_2](A^{n-})_{x/n}\cdot mH_2O$. A unique structural characteristic of LDH materials is that the M^{2+} and M^{3+} cations are distributed in a highly-ordered state in the hydroxide layers. Recently, considerable interest has been focused on LDH materials as catalysts, catalyst supports or precursors by virtue of their versatility in terms of chemical composition and structural architecture.[9] Compared with traditional supported catalysts, LDH-based catalysts show the following advantages: (1) if a LDH precursor contains transition metal ions, they can be *in situ* reduced to give catalytically-active metal nanoparticles anchoring to a

[a] *State Key Laboratory of Chemical Resource Engineering, Beijing University of Chemical Technology, Beijing, 100029, China. E-mail: vh30@163.com, weimin@mail.buct.edu.cn; Fax: +86 10 64425385; Tel: +86 10 64412131*
[b] *Beijing Research Institute of Chemical Industry, Sinopec Group, Beijing 100013, PR China*

† Electronic supplementary information (ESI) available. See DOI: 10.1039/c5cy02026c

so-called mixed metal oxide phase, with high dispersion and stability; (2) if a proportion of alkaline elements (*e.g.*, Mg) is further introduced into a LDH precursor, a tunable alkaline site structure can be obtained. Therefore, it is a promising strategy for fabricating alkaline-assisted metal nanocatalysts with enhanced cooperative catalysis.

In this work, alkaline-assisted Ni nanocatalysts supported on Mg/Al mixed metal oxides (denoted as $Ni_x/Mg_{2-x}Al$-MMO) were successfully prepared by a facile reduction treatment upon the $Ni_xMg_{2-x}Al$-LDH precursors, and their catalytic performance toward CO_2 methanation was studied in detail. The Ni/MgAl-MMO catalyst shows the best catalytic behavior with a CO_2 conversion of 97.9% and selectivity of 97.5% (250 °C), which serves as a promising candidate for the substitution of noble metal catalysts. Based on the XRD, HRTEM, H_2 chemisorption and *in situ* CO-FTIR results, it is found that the TOF value with respect to the exposed Ni atom (TOF_{Ni}) increases gradually with the increment of the density of MgO base sites, although these $Ni_x/Mg_{2-x}Al$-MMO catalysts show a rather close average Ni particle size. This verifies that the cooperative catalysis between the Ni sites and MgO base sites accounts for the enhanced low-temperature reaction activity. Moreover, *in situ* DRIFTS reveals that MgO participates in this reaction by effectively activating CO_2, while Ni provides H-species for further hydrogenation of activated CO_2. This work demonstrates a successful paradigm for the development of tunable base sites, which play a key role in obtaining an optimal cooperative effect in CO_2 methanation.

2. Experimental section

2.1 Materials

$Ni(NO_3)_2{\cdot}6H_2O$, $Mg(NO_3)_2{\cdot}6H_2O$ and $Al(NO_3)_3{\cdot}9H_2O$ were purchased from Sigma-Aldrich. Other chemicals including NaOH and Na_2CO_3 were purchased from Beijing Chemical Co., LTD., and deionized water was used in all the experimental processes.

2.2 Synthesis of $Ni_xMg_{2-x}Al$-LDH precursors and $Ni_x/Mg_{2-x}Al$-MMO catalysts

The $Ni_xMg_{2-x}Al$-LDH precursors with tunable compositions were synthesized by using a method that involves separate nucleation and aging steps (SNAS) developed in our laboratory.[10] Typically, $Ni(NO_3)_2{\cdot}6H_2O$, $Mg(NO_3)_2{\cdot}6H_2O$ and $Al(NO_3)_3{\cdot}9H_2O$ with various molar ratios of Ni^{2+}/Mg^{2+} were dissolved in 100 mL of deionized water to give a solution with a total cationic concentration of 0.15 M (solution A). A certain amount of NaOH and Na_2CO_3 were dissolved together to obtain 100 mL of a base solution (solution B: $[CO_3^{2-}] = 2.0[M^{3+}]$, $[OH^-] = 1.8([M^{2+}] + [M^{3+}])$). Solution A and B were then mixed together at a steady rate of 3000 rpm for 1 min. The resulting suspension was aged in a sealed Teflon autoclave at 110 °C for 48 h. The obtained precipitate was washed thoroughly with water and ethanol and dried in an oven at 60 °C overnight. Finally, the obtained $Ni_xMg_{2-x}Al$-LDH precursor was reduced under a H_2/N_2 (1/9, *v*/*v*) stream at a reduction temperature of 500 °C for 4 h, with a heating rate of 5 °C min^{-1}. The reduction process results in the phase transformation from $Ni_xMg_{2-x}Al$-LDH to metallic Ni nanoparticles supported on MgO-Al_2O_3 mixed metal oxides (denoted as $Ni_x/Mg_{2-x}Al$-MMO).

2.3 Synthesis of Ni/CNT, Ni/Al_2O_3 and Ni/MgO catalysts

In order to carry out a comparison study, supported Ni catalysts on three substrates (carbon nanotubes CNTs, Al_2O_3, MgO) as reference samples were synthesized by an impregnation method. In detail, the support (3.0 g) was dispersed into $Mg(NO_3)_2{\cdot}6H_2O$ solution (2.2230 g, 5.0 mL). After agitation for 3 h, the resulting slurry was dried at 60 °C for 4 h, followed by calcination in air at 400 °C for 3 h. Finally, the calcined sample was reduced under a H_2/N_2 (1/9, *v*/*v*) stream at 500 °C for 4 h, with a heating rate of 5 °C min^{-1}, which was denoted as Ni/CNT, Ni/Al_2O_3 and Ni/MgO catalyst, respectively.

2.4 Characterization

X-ray diffraction (XRD) patterns of the samples were obtained on a Rigaku XRD-6000 diffractometer, using Cu Kα radiation (λ = 0.154 nm) at 40 kV, 40 mA, a scanning rate of 10° min^{-1}, a step size of 0.02° s^{-1}, and a 2θ angle ranging from 3 to 70°. The morphology of the samples was investigated using a Zeiss Supra 55 scanning electron microscope (SEM) with an accelerating voltage of 20 kV. Metal elements analysis was carried out using a Shimadzu ICPS-7500 inductively coupled plasma–atomic emission spectrometer (ICP–AES). Low-temperature N_2 adsorption-desorption experiments were carried out using a Quantachrome Autosorb-1C-VP instrument. Prior to N_2 adsorption, the sample was outgassed at 200 °C overnight to desorb moisture on the surface of the sample. The total specific surface area was evaluated using the multipoint Brunauer-Emmett-Teller (BET) method. High-resolution electron microscopy (HRTEM) observations were carried out on a JEM-2100 transmission electron microscope. Hydrogen temperature programmed reduction (H_2-TPR) and hydrogen temperature programmed desorption (H_2-TPD) were conducted in a quartz tube reactor on a Micromeritics ChemiSorb 2720 with a thermal conductivity detector (TCD). In a typical H_2-TPR process, 100 mg of a sample placed in a quartz tube reactor was first degassed under flowing argon at 400 °C for 2 h and cooled down to room temperature. Then, a gaseous mixture of H_2 and Ar (1 : 9, *v*/*v*) was fed to the reactor at 50 mL min^{-1}. The temperature was raised to 700 °C at a heating rate of 10 °C min^{-1}. For the H_2-TPD process, 100 mg of the reduced sample was first sealed and calcined in a reactor in a gaseous mixture of H_2 and Ar (1 : 9, *v*/*v*) at 400 °C for 1 h. Subsequently, the catalyst was purged in Ar at 500 °C for 30 min to remove excess hydrogen, then cooled down to 25 °C for readsorption of H_2. Finally, the sample was placed under a stream of argon with rate of 50 mL min^{-1} and a temperature ramp of 10 °C min^{-1} to perform TPD.

In situ Fourier transform infrared absorption spectroscopy of adsorbed CO was carried out in a quartz cell equipped with KBr windows allowing sample activation and successive measurements in the range of 25–600 °C, at a pressure as low as 10^{-4}. About 50 mg of the sample was pressed into a disk and activated in the same cell used for the measurements. FTIR spectra were collected with a Nicolet 380 spectrophotometer instrument at a spectra resolution of 4 cm^{-1} and accumulation of 64 scans. After treatment in hydrogen at 400 °C for 1 h, the sample was purged in Ar at 500 °C for 30 min to remove excess hydrogen and then cooled to 50 °C and scanned to get a background record below a pressure of 2×10^{-4} Pa. Then, the sample was exposed to a CO flow at 50 °C for another 120 min. Sample scanning for adsorbed CO was conducted after the pressure was reduced below 2×10^{-4} Pa again.

In situ diffuse reflectance Fourier transform infrared spectroscopy (*in situ* DRIFTS) was carried out on an *in situ* reaction cell. The spectra were collected in a Magna 6700 spectrometer equipped with a MCT narrow-band detector. The reaction gas mixture was introduced into the reaction cell *via* mass flow controllers. Prior to the experiments, the catalyst was heated up under a H_2/N_2 (1/9, *v*/*v*) stream to 500 °C for 2 h, and then cooled down to 170 °C for the background spectra collection. The methanation of CO_2 over the catalyst occurred with the introduction of a $^{12}CO_2$-containing reaction gas mixture into the *in situ* cell. After the spectra signals reached saturation, the $^{12}CO_2$ gas was switched to $^{13}CO_2$ for further spectra collection.

2.5 Catalytic evaluation

The catalytic performance of the nickel-based catalysts was evaluated under atmospheric pressure in a fixed-bed quartz reactor with an interior diameter of 8 mm. The reactor was heated in a tube furnace equipped with a temperature controller, and all gases were monitored by calibrated mass flow controllers. Prior to the catalytic performance test, 0.5 g of the catalyst was first pretreated in a gaseous mixture of H_2/N_2 (1/9, *v*/*v*) for 1 h with a total gas flow of 100 mL min^{-1} at 500 °C with a heating rate of 5 °C min^{-1}, and then cooled to 100 °C in nitrogen. Subsequently, a mixture of H_2, CO_2 and Ar (an internal standard) with a molar ratio of $H_2 : CO_2 : Ar = 12 : 3 : 5$ was introduced into the reactor with a total flux of 40 mL min^{-1}. The gas hourly space velocity (GHSV) was maintained at 2400 h^{-1}. The composition of the outlet gases was analyzed online using a GC-2014C gas chromatograph equipped with a TCD detector and FID detector. The CO_2 conversion (eqn (1)) and CH_4 selectivity (eqn (2)) are defined as follows:

$$\text{Conversion}_{CO_2}(\%) = \left(1 - \frac{S_{\text{out}(CO_2)} S_{\text{in(Ar)}}}{S_{\text{in}(CO_2)} S_{\text{out(Ar)}}}\right) \times 100 \quad (1)$$

$$\text{Selectivity}_{CH_4}(\%) = \frac{c_{(CH_4)}}{0.15 \times \left(\frac{S_{\text{out(Ar)}}}{S_{\text{in(Ar)}}} - \frac{S_{\text{out}(CO_2)}}{S_{\text{in}(CO_2)}}\right)} \times 100 \quad (2)$$

where $S_{\text{in}(CO_2)}$ and $S_{\text{out}(CO_2)}$ are the peak areas of CO_2 in the inlet and outlet gas determined by gas chromatography; $S_{\text{in(Ar)}}$ and $S_{\text{out(Ar)}}$ are the peak areas of Ar in the inlet and outlet gas; $c_{(CH_4)}$ is the methane concentration in the outlet gas, which is calculated based on the external standard method.

Furthermore, the reaction rate (R) of the $Ni_x/Mg_{2-x}Al$-MMO catalysts (eqn (3)) is evaluated at a low reaction temperature (170 °C) and low level of CO_2 conversion (<20%), to minimize the effects of transport and water inhibition. The reaction rate is calculated based on the following equation:

$$R = \frac{V \times C \times 10^{-3}}{m \times V_m} \quad (3)$$

where V refers the volume of CO_2 fed into the reaction per minute (mL min^{-1}); C is the conversion of CO_2 at 170 °C; m denotes the weight of the catalyst (g), and V_m is the molar volume of CO_2 (22.4 L mol^{-1}).

3. Results and discussion

3.1 Structural and morphological study of the catalysts

The $Ni_xMg_{2-x}Al$-LDH precursors with various Ni/Mg ratios (1/4, 2/3, 1/1 and 4/1) were synthesized *via* a co-precipitation method. Their XRD patterns (Fig. S1A†) show characteristic reflections at 2θ ~12°, ~24° and ~35°, which can be indexed to (003), (006) and (012) of an LDH phase, respectively.[11] After reduction of the $Ni_xMg_{2-x}Al$-LDH precursors at 500 °C for 4 h, the corresponding Ni-based catalysts supported on Mg/Al mixed metal oxides (typically, crystalline MgO and amorphous Al_2O_3) were obtained (denoted as $Ni_x/Mg_{2-x}Al$-MMO). Fig. S1B† shows the XRD patterns of the resulting $Ni_x/Mg_{2-x}Al$-MMO samples. Typical (200) and (220) reflections of face-centered MgO (JCPDS card no. 33–0664) at 2θ ~43° and 63° are observed in all these samples, while no characteristic reflection of metal Ni is found, indicative of a small particle size of the resulting Ni species. Moreover, the content of metal elements in these samples as well as the loading of Ni determined by using an inductively coupled plasma–atomic emission spectrometer (ICP–AES) are summarized in Table 1. The determined ratio of the total divalent to trivalent metal is maintained to be ~2 : 1 with Ni loading ranging from 17.2% to 57.8%, close to the nominal ones.

HRTEM measurements were performed to investigate the structure and distribution of Ni species in these $Ni_x/Mg_{2-x}Al$-MMO samples (Fig. 1). It is observed that the Ni nanoparticles are highly dispersed within the Mg/Al mixed metal oxides. Notably, with the enhancement of the Ni/Mg molar ratio from 1/4 to 4/1, the density of the Ni nanoparticles increases gradually, but their average size remains almost unchanged (~2.5 nm). The corresponding HRTEM images with a high magnification further reveal a characteristic

Table 1 Structural parameters of various samples

Catalysts	S_{BET} (m^2g^{-1})	Ni[a] (wt%)	Molar ratio[a] (Ni/Mg/Al)	Ni dispersion[b] (%)	$n_{surface\ Ni}$[b] (mmol g^{-1}_{cat})	$n_{CO_2,Mg}$[c] (mmol g^{-1}_{cat})	$n_{CO_2,Al}$[c] (mmol g^{-1}_{cat})	Mean Ni particle size by TEM (nm)
$Ni_{0.4}/Mg_{1.6}Al$-MMO	178	17.2	0.41/1.60/1.00	21.7	0.64	0.15	0.08	2.4 ± 0.3
$Ni_{0.8}/Mg_{1.2}Al$-MMO	172	27.6	0.64/1.18/1.00	22.3	1.05	0.11	0.08	2.4 ± 0.2
Ni/MgAl-MMO	161	36.9	0.98/1.00/1.00	21.3	1.34	0.09	0.07	2.5 ± 0.3
$Ni_{1.6}/Mg_{0.4}Al$-MMO	157	57.8	1.56/0.40/1.00	19.8	1.94	0.03	0.07	2.5 ± 0.3
Ni/CNT	412	36.6	—	9.80	0.61	—	—	7.1 ± 1.6
Ni/Al_2O_3	41	37.4	—	11.2	0.71	—	0.07	5.2 ± 1.0
Ni/MgO	33	37.8	—	14.6	0.95	0.12	—	4.0 ± 0.8

[a] Values determined by ICP–AES. [b] Values calculated based on H_2 chemisorption.[2c,12] [c] Values calculated based on CO_2-TPD.

lattice spacing of 0.204 nm for these nanoparticles, which is indexed to the (111) plane of fcc Ni. In addition, for comparison, Ni particles supported on three substrates (carbon nanotubes (CNTs), Al_2O_3 and MgO) were also prepared by the impregnation method, with a Ni loading comparable to that of the Ni/MgAl-MMO sample (37%). The resulting Ni/CNT, Ni/Al_2O_3 and Ni/MgO catalysts are characterized by random packing of Ni nanoparticles with an irregular shape and very broad particle size distribution (as shown in Fig. S2†).

Hydrogen temperature programmed reduction (H_2-TPR) measurements were carried out to provide information on the redox properties of Ni/MgAl-MMO, Ni/CNT, Ni/Al_2O_3 and Ni/MgO, respectively (Fig. 2). For the Ni/CNT, Ni/Al_2O_3 and Ni/MgO reference samples, two reduction peaks in the range of 220–450 °C are observed, which are assigned to the reduction of bulk NiO (low temperature) and highly-dispersed NiO species (high temperature), respectively.[13] However, in the case of Ni/MgAl-MMO, only one unique and symmetric peak at a relatively high temperature (~435 °C) is identified, indicating a relatively hard to reduce Ni^{2+} species with good uniformity in the LDH precursor.[14] This is related to the fact that Ni^{2+} is well diluted/isolated by the Mg^{2+} and Al^{3+} cations in the LDH lamellar. Moreover, the H_2 chemisorption capacities of the synthesized $Ni_x/Mg_{2-x}Al$-MMO, Ni/CNT, Ni/Al_2O_3 and Ni/MgO were further measured to obtain the specific Ni dispersion (Table 1). The four $Ni_x/Mg_{2-x}Al$-MMO samples show a comparable dispersion degree of ~20% owing to their rather close particle size, which is higher than those of Ni/CNT, Ni/Al_2O_3 and Ni/MgO samples (9.8%–14.6%). This is in accordance with the results of TEM. In addition, the surface structure of the Ni particles in the four $Ni_x/Mg_{2-x}Al$-MMO samples was also studied by *in situ* infrared spectroscopy of adsorbed CO (as shown in Fig. 3). Two typical CO adsorption peaks (at ~2050 cm^{-1} and ~1950 cm^{-1}) with a rather close

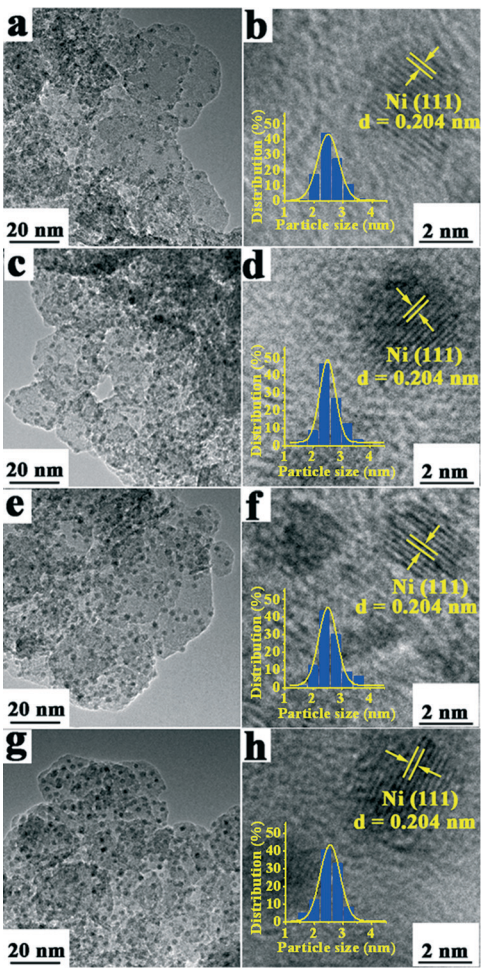

Fig. 1 HRTEM images of the $Ni_x/Mg_{2-x}Al$-MMO samples: (a, b) $Ni_{0.4}/Mg_{1.6}Al$-MMO, (c, d) $Ni_{0.8}/Mg_{1.2}Al$-MMO, (e, f) Ni/MgAl-MMO and (g, h) $Ni_{1.6}/Mg_{0.4}Al$-MMO. The inset in (b), (d), (f) and (h) is the corresponding particle-size frequency distribution histogram (400 particles analyzed).

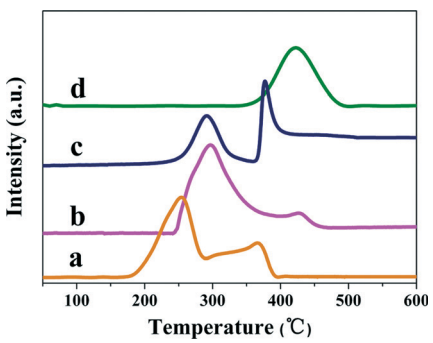

Fig. 2 H_2-TPR profiles of the (a) Ni/CNT, (b) Ni/Al_2O_3, (c) Ni/MgO and (d) Ni/MgAl-MMO samples.

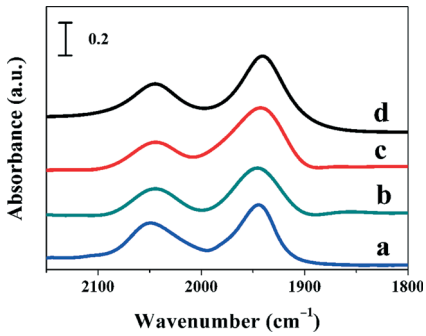

Fig. 3 *In situ* FTIR spectra of CO adsorption of the four $Ni_x/Mg_{2-x}Al$-MMO samples: (a) $Ni_{0.4}/Mg_{1.6}Al$-MMO, (b) $Ni_{0.8}/Mg_{1.2}Al$-MMO, (c) Ni/MgAl-MMO and (d) $Ni_{1.6}/Mg_{0.4}Al$-MMO.

intensity are observed, which are attributed to the linearly absorbed and bridge-bonded CO on the Ni atoms,[15] respectively. This implies that the Ni particles in these four $Ni_x/Mg_{2-x}Al$-MMO samples possess a similar surface structure.

The structure of the base sites of the $Ni_x/Mg_{2-x}Al$-MMO, Ni/CNT, Ni/Al_2O_3 and Ni/MgO samples was investigated by using CO_2-TPD (Fig. 4). For the Ni/CNT sample, no obvious CO_2 desorption peak is observed, indicative of the absence of base sites on the CNT support. In contrast, the Ni/Al_2O_3 sample shows one low-temperature peak at ~120 °C, which is associated with weak base sites, while Ni/MgO displays one medium-temperature peak at ~220 °C, corresponding to moderately strong base sites. Notably, all the four $Ni_x/Mg_{2-x}Al$-MMO samples exhibit two peaks at ~120 °C and 220 °C, which are assigned to the adsorbed CO_2 on the Al_2O_3 phase and MgO phase, respectively. Moreover, from $Ni_{1.6}/Mg_{0.4}Al$-MMO to $Ni_{0.4}/Mg_{1.6}Al$-MMO, the peak intensity (namely the capacity) of the adsorbed CO_2 on MgO increases gradually while that of the adsorbed CO_2 on Al_2O_3 remains at a comparable level. This is consistent with the evolution of MgO and Al_2O_3 in these $Ni_x/Mg_{2-x}Al$-MMO samples. In addition, the amount of adsorbed CO_2 on MgO and Al_2O_3 per gram of sample (denoted as $n_{CO_2,Mg}$ and $n_{CO_2,Al}$, respectively), is calculated by CO_2-TPD (Table 1). For the $Ni_x/Mg_{2-x}Al$-MMO samples, as the Mg/Ni molar ratio rises from 1/4 to 4/1, the value of $n_{CO_2,Mg}/(n_{CO_2,Mg} + n_{CO_2,Al})$ increases gradually, indicating an enhanced medium–strong basic strength.

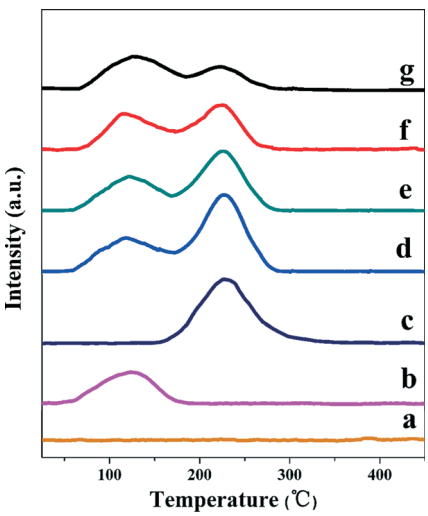

Fig. 4 CO_2-TPD profiles of the synthesized Ni samples: (a) Ni/CNT, (b) Ni/Al_2O_3, (c) Ni/MgO, (d) $Ni_{0.4}/Mg_{1.6}Al$-MMO, (e) $Ni_{0.8}/Mg_{1.2}Al$-MMO, (f) Ni/MgAl-MMO and (g) $Ni_{1.6}/Mg_{0.4}Al$-MMO.

3.2 Evaluation of catalytic behavior

The catalytic performance of the Ni/MgAl-MMO, Ni/CNT, Ni/Al_2O_3 and Ni/MgO catalysts toward the reaction of CO_2 methanation was studied. Fig. 5A displays CO_2 conversion as a function of reaction temperature. The values of T_{50}, corresponding to the temperature at which 50% conversion is obtained, are 195, 263, and 306 °C for Ni/MgAl-MMO, Ni/MgO and Ni/Al_2O_3, respectively. Moreover, it is found that the maximal levels of CO_2 conversion in the presence of the Ni/Al_2O_3 and Ni/MgO catalysts are only 79.1 and 89.0% (at ~350 °C), respectively. In the case of the Ni/MgAl-MMO catalyst, however, CO_2 conversion exceeds 80% at 220 °C and reaches the maximal value (97.9%) at 250 °C, which is far superior to the catalytic activity of supported noble-metal and Ni-based catalysts reported previously.[2c,9b,16] Ni/MgAl-MMO clearly exhibits significantly enhanced low-temperature activity for CO_2 methanation. Fig. 5B also shows the corresponding selectivity toward CH_4 as a function of reaction temperature over the Ni/MgAl-MMO, Ni/A_2O_3 and Ni/MgO catalysts. As can be seen, the selectivity to CH_4 over the three catalysts is satisfactory (>95%) at the low temperature region; however, a slight decrease for the latter two samples above 300

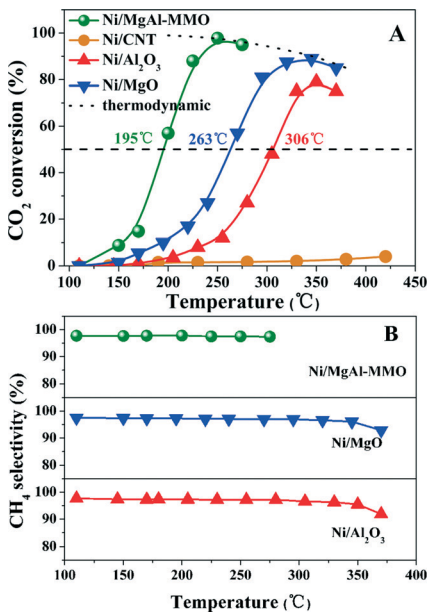

Fig. 5 (A) CO_2 methanation at steady state as a function of reaction temperature over the as-prepared Ni/MgAl-MMO, Ni/CNT, Ni/Al_2O_3 and Ni/MgO catalysts (GHSV: 2400 h^{-1}). (B) The corresponding selectivity toward CH_4 as a function of reaction temperature.

°C is observed, possibly due to the occurrence of side reactions (*e.g.*, reverse water-gas shift[17] and reforming reaction[18]). Notably, the Ni/CNT sample almost suffers from inactivation along the whole reaction temperature, which suggests that the base site of the support plays an important role in the catalytic process of CO_2 methanation.

The series of $Ni_x/Mg_{2-x}Al$-MMO catalysts provide a good model to investigate the effect of base sites on CO_2 methanation due to their parallel morphology and the surface structure of the Ni particles. To establish the structure–activity relationship, the reaction rates of the $Ni_x/Mg_{2-x}Al$-MMO catalysts (listed in Table 2) were evaluated at low reaction temperature (170 °C) and level of CO_2 conversion (<20%), to minimize the effects of transport and water inhibition. As shown in Fig. 6A, the correlation between the reaction rate and the Mg/Ni molar ratio of the $Ni_x/Mg_{2-x}Al$-MMO catalysts displays a volcano-like shape along with the increase in Mg/Ni ratio, with the maximum reaction rate obtained for the Ni/MgAl-MMO catalyst. This suggests that cooperative catalysis between the Ni sites and the MgO base sites occurs in CO_2 methanation, which determines the catalytic activity. Subsequently, the TOF values with respect to the exposed Ni atom (TOF_{Ni}) are calculated for these samples, which increase in the following order: $Ni_{1.6}/Mg_{0.4}Al$-MMO (6.68×10^{-4} s^{-1}) < Ni/MgAl-MMO (10.8×10^{-4} s^{-1}) < $Ni_{0.8}/Mg_{1.2}Al$-MMO (12.0×10^{-4} s^{-1}) < $Ni_{0.4}/Mg_{1.6}Al$-MMO (13.8×10^{-4} s^{-1}). Although these $Ni_x/Mg_{2-x}Al$-MMO catalysts possess Ni nanoparticles with a very close average size and surface structure, their TOF_{Ni} values are rather different. Furthermore, the relationship between the TOF_{Ni} value and the density of the MgO base site for these $Ni_x/Mg_{2-x}Al$-MMO catalysts is studied (Fig. 6B), which shows a linear correlation. This further confirms the cooperative catalysis between the Ni active site and the MgO base site. The four $Ni_x/Mg_{2-x}Al$-MMO catalysts with Ni nanoparticles having a very similar surface structure show rather different TOF_{Ni} values, indicating that the Ni–MgO interfacial site plays an important role in cooperatively catalyzing CO_2 methanation. By virtue of the tunable chemical composition of the LDH precursors, largely enhanced low-temperature activity is obtained over the Ni/MgAl-MMO catalyst, which is likely attributed to the optimized cooperative effect between Ni and the base site. In addition, the long-term catalytic stability of the Ni/MgAl-MMO catalyst was also investigated. As shown in Fig. S3A,† CO_2 conversion remains almost constant during 100 h on stream. No obvious change in morphology and structure is observed after 100 h of stability test (Fig. S3B†), demonstrating an effective and stable catalyst.

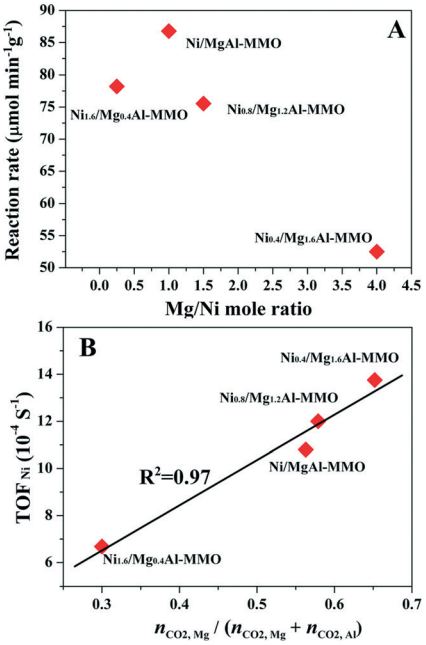

Fig. 6 (A) Correlation between the reaction rate and the Mg/Ni molar ratio for the $Ni_x/Mg_{2-x}Al$-MMO catalysts (reaction conditions: 170 °C, GHSV = 2400 h^{-1}, CO_2 conversion <20%). (B) Relationship between the TOF_{Ni} value and the concentration of base sites in the $Ni_x/Mg_{2-x}Al$-MMO catalysts.

To give a deep insight into the mechanism of cooperative catalysis, CO_2 methanation over the Ni/CNT and Ni/MgAl-MMO catalysts was further investigated by steady-state isotope transient kinetic analysis (SSITKA)-type *in situ* DRIFT infrared spectroscopy. After 60 min of reaction at 170 °C, CO_2 was replaced by its isotopic gas ($^{13}CO_2$) for another 60 min of reaction. By correlating the buildup/decay of various surface species including CO, hydrocarbonate and carbonate, detailed information on the catalytic reaction mechanism can be obtained. Fig. 7A shows that once the reaction gas mixture is introduced, typical signals for the gas phase CO_2 (2361 and

Table 2 Catalytic performance of various catalysts[a]

Catalysts	T^b (°C)	Conv.[b] (%)	Sel.[b] (%)	T_{50} (°C)	R^c (μmol min^{-1} g^{-1})	TOF_{Ni} ($\times 10^{-4}$ s^{-1})
$Ni_{0.4}/Mg_{1.6}Al$-MMO	300	95.1	96.9	241	52.5	13.8
$Ni_{0.8}/Mg_{1.2}Al$-MMO	280	96.7	97.1	221	75.5	12.0
Ni/MgAl-MMO	250	97.9	97.5	195	86.7	10.8
$Ni_{1.6}/Mg_{0.4}Al$-MMO	270	96.5	97.1	210	78.2	6.68
Ni/CNT	—	—	—	—	—	—
Ni/Al_2O_3	350	79.1	95.5	306	16.1	3.75
Ni/MgO	345	89.0	96.1	263	29.5	5.22

[a] Reaction conditions: catalyst (0.5 g), GHSV (2400 h^{-1}). [b] The results are obtained at the maximum conversion of CO_2. T_{50} refers to the reaction temperature at which a CO_2 conversion of 50% is obtained. [c] Values are calculated based on the amount of CO_2 per minute per gram of catalyst.

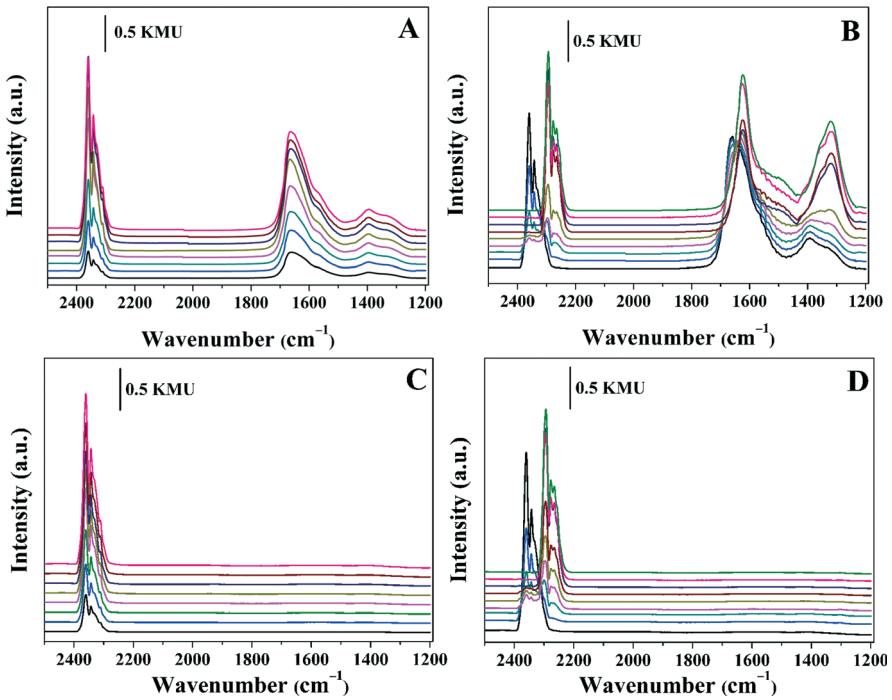

Fig. 7 DRIFT spectra recorded at 170 °C during 60 min with $^{12}CO_2$ as the reaction gas and subsequent 60 min reaction by introducing $^{13}CO_2$ over: (A, B) Ni/MgAl-MMO and (C, D) Ni/CNT. From bottom to top: (A, C) 0.5, 1.5, 3, 5, 10, 20, 40 and 60 min; (B, D) 0, 0.5, 1.5, 3, 5, 10, 20, 40 and 60 min.

2343 cm^{-1}), carbonate (1392 cm^{-1}) and hydrocarbonate (1662 cm^{-1}) are identified immediately over the Ni/MgAl-MMO catalyst. These bands are almost saturated over 60 min. No obvious signal assigned to CH_4 (3016 cm^{-1}) is observed, probably due to weak adsorption on the catalyst surface. When the $^{12}CO_2$ stream is switched to $^{13}CO_2$ gas, significant changes occur in the DRIFT spectra (Fig. 7B). The bands of $^{12}CO_{2,gas}$ diminish gradually, while new bands attributed to $^{13}CO_{2,gas}$ (2295, 2278 and 2267 cm^{-1}) are observed. The characteristic bands of carbonate (1392 cm^{-1}) and hydrocarbonate (1662 cm^{-1}) display a similar decrease as $^{12}CO_{2,gas}$, while the corresponding new bands due to ^{13}C-carbonate (1317 cm^{-1}) and ^{13}C-hydrocarbonate (1624 cm^{-1}) grow steadily. This indicates that carbonate and hydrocarbonate are intermediates in the main reaction path. In contrast, in the case of the Ni/CNT catalyst without a base site, the formation of any relevant intermediates during the introduction of feed gas is hardly observed (Fig. 7C and D). The results above indicate that the activation of CO_2 molecules to carbonate/hydrocarbonate species is critical for CO_2 methanation, which is achieved by MgO base sites. Although CO_2 is very chemically stable, base sites can activate it to carbonate/hydrocarbonate species at appreciable rates, which has been confirmed by previous studies on pure alkaline supports.[5b,7] It is reported that metal catalysts provide reactive H-species (through H_2 activation) to hydrogenate carbonate at a temperature far below the uncatalyzed hydrogenation temperature.[7] Therefore, a cooperative catalytic mechanism is proposed for the alkaline-assisted Ni-based catalyst, in which the Ni site and the base site serve as active centers toward H_2 activation (dissociation of H_2) and CO_2 activation, respectively, followed by subsequent hydrogenation to give methane. Notably, the spillover of dissociated H on a MgO surface is rather difficult, according to the valence band theory in which a hydrogen atom does not bond to a solid surface with saturated atoms (*e.g.*, MgO, SiO_2 and Al_2O_3).[19] It is thus proposed that the Ni/MgO interfacial sites act as dual active centers to cooperatively catalyze the conversion of CO_2 to methane. Moreover, among the four $Ni_x/Mg_{2-x}Al$-MMO samples, the Ni/MgAl-MMO catalyst (molar ratio of Ni/Mg close to 1 : 1) shows a moderate active site density (as shown in Table 1), which likely induces the optimal tradeoff between H_2 activation and CO_2 activation. This promotes subsequent hydrogenation of the carbonate species to produce methane, and the highest activity is therefore obtained over Ni/MgAl-MMO.

4. Conclusions

In summary, highly-dispersed Ni catalysts supported on MgO-Al_2O_3 mixed metal oxides were successfully synthesized *via* the topotactic transformation of $Ni_xMg_{2-x}Al$-LDH precursors with various Ni/Mg molar ratios. The resulting $Ni_x/Mg_{2-x}Al$-MMO catalysts are evaluated by the hydrogenation of CO_2 to methane, and the Ni/MgAl-MMO sample shows largely enhanced catalytic behavior (CO_2 conversion: 97.9%, CH_4 selectivity: 97.5%, reaction temperature: 250 °C). Both the kinetic study and the time-resolved DRIFTS measurements equipped with SSITKA demonstrate that the base site of MgO serves as an active center to activate CO_2 to carbonate/hydrocarbonate. Therefore, a cooperative catalytic mechanism occurring

at the Ni species/MgO interface is proposed for this alkaline-assisted Ni-based catalyst, which is optimized in the Ni/MgAl-MMO catalyst, accounting for its excellent low-temperature activity toward CO_2 methanation.

Acknowledgements

This work was supported by the 973 Program (Grant No. 2014CB932104), the National Natural Science Foundation of China, the Fundamental Research Funds for the Central Universities (YS 1406) and the Research on the Chemical Industry Cluster and the Socioeconomic Coordinated Development of Xinjiang (Grant No. JX20140015).

Notes and references

1 (*a*) J. M. Bermúdez, B. Fidalgo, A. Arenillas and J. A. Menéndez, *Fuel*, 2012, **94**, 197–203; (*b*) R. Razzaq, H. W. Zhu, L. Jiang, U. Muhammad, C. S. Li and S. J. Zhang, *Ind. Eng. Chem. Res.*, 2013, **52**, 2247–2256; (*c*) Z. F. Qin, J. Ren, M. Q. Miao, Z. Li, J. Y. Lin and K. C. Xie, *Appl. Catal., B*, 2015, **164**, 18–30.

2 (*a*) W. Wang, S. P. Wang, X. B. Ma and J. L. Gong, *Chem. Soc. Rev.*, 2011, **40**, 3703–3727; (*b*) P. Gao, F. Li, F. K. Xiao, N. Zhao, N. N. Sun, W. Wei, L. S. Zhong and Y. H. Sun, *Catal. Sci. Technol.*, 2012, **2**, 1447–1454; (*c*) J. Liu, C. M. Li, F. Wang, S. He, H. Chen, Y. F. Zhao, M. Wei, D. G. Evans and X. Duan, *Catal. Sci. Technol.*, 2013, **3**, 2627–2633; (*d*) S. Sharma, Z. P. Hu, P. Zhang, E. W. McFarland and H. Metiu, *J. Catal.*, 2011, **278**, 297–309.

3 (*a*) R. G. Zhang, H. Y. Liu, B. J. Wang and L. X. Ling, *Appl. Catal., B*, 2012, **126**, 108–120; (*b*) D. C. Upham, A. R. Derk, S. Sharma, H. Metiu and E. W. McFarland, *Catal. Sci. Technol.*, 2015, **5**, 1783–1791; (*c*) A. Karelovic and P. Ruiz, *ACS Catal.*, 2013, **3**, 2799–2812; (*d*) M. A. A. Aziz, A. A. Jalil, S. Triwahyono, R. R. Mukti, Y. H. Taufiq-Yap and M. R. Sazegar, *Appl. Catal., B*, 2014, **147**, 359–368; (*e*) Q. S. Pan, J. X. Peng, S. Wang and S. D. Wang, *Catal. Sci. Technol.*, 2014, **4**, 502–509.

4 (*a*) A. Westermann, B. Azambre, M. C. Bacariza, I. Graça, M. F. Ribeiro, J. M. Lopes and C. Henriques, *Appl. Catal., B*, 2015, **174**, 120–125; (*b*) H. Takano, H. Shinomiya, K. Izumiya, N. Kumagai, H. Habazaki and K. Hashimoto, *Int. J. Hydrogen Energy*, 2015, **40**, 8347–8355; (*c*) W. L. Zhen, B. Li, G. X. Lu and J. T. Ma, *Chem. Commun.*, 2015, **51**, 1728–1731; (*d*) A. Borgschulte, E. Callini, N. Stadie, Y. Arroyo, M. D. Rossell, R. Erni, H. Geerlings, A. Züttel and D. Ferri, *Catal. Sci. Technol.*, 2015, **5**, 4613–4621; (*e*) M. A. A. Aziz, A. A. Jalil, S. Triwahyono and A. Ahmad, *Green Chem.*, 2015, **17**, 2647–2663.

5 (*a*) Q. S. Pan, J. X. Peng, T. J. Sun, S. Wang and S. D. Wang, *Catal. Commun.*, 2014, **45**, 74–78; (*b*) J. Park and E. W. McFarland, *J. Catal.*, 2009, **266**, 92–97; (*c*) M. Guo and G. X. Lu, *RSC Adv.*, 2014, **4**, 58171–58177; (*d*) Y. R. Li, G. X. Lu and J. T. Ma, *RSC Adv.*, 2014, **4**, 17420–17428.

6 (*a*) A. F. Gusovius and R. Prins, *J. Catal.*, 2002, **211**, 273–277; (*b*) L. F. Liotta, G. Deganello, P. Delichere, C. Leclercq and G. A. Martin, *J. Catal.*, 1996, **164**, 334–340; (*c*) M. J. Climent, A. Corma, S. Iborra, K. Epping and A. Velty, *J. Catal.*, 2004, **225**, 316–326; (*d*) B. Veldurthy, J. M. Clacens and F. Figueras, *J. Catal.*, 2005, **229**, 237–242.

7 H. Y. Kim, H. M. Lee and J. N. Park, *J. Phys. Chem. C*, 2010, **114**, 7128–7131.

8 (*a*) Q. Wang and D. O'Hare, *Chem. Rev.*, 2012, **112**, 4124–4155; (*b*) C. M. Li, M. Wei, D. G. Evans and X. Duan, *Small*, 2014, **10**, 4469–4486; (*c*) J. Liang, R. Ma, N. Iyi, Y. Ebina, K. Takada and T. Sasaki, *Chem. Mater.*, 2010, **22**, 371–378.

9 (*a*) J. A. Gursky, S. D. Blough, C. Luna, C. Gomez, A. N. Luevano and E. A. Gardner, *J. Am. Chem. Soc.*, 2006, **128**, 8376–8377; (*b*) S. He, C. M. Li, H. Chen, D. S. Su, B. S. Zhang, X. Z. Cao, B. Y. Wang, M. Wei, D. G. Evans and X. Duan, *Chem. Mater.*, 2013, **25**, 1040–1046; (*c*) J. Liu, S. M. Xu, W. H. Bing, F. Wang, C. M. Li, M. Wei, D. G. Evans and X. Duan, *ChemCatChem*, 2015, **7**, 846–855; (*d*) H. C. Liu and E. Min, *Green Chem.*, 2006, **8**, 657–662; (*e*) R. D. Hetterley, R. Mackey, J. T. A. Jones, Y. Z. Khimyak, A. M. Fogg and L. V. Kozhevnikov, *J. Catal.*, 2008, **258**, 250–255.

10 Y. Zhao, F. Li, R. Zhang, D. G. Evans and X. Duan, *Chem. Mater.*, 2002, **14**, 4286–4291.

11 J. Pisson, C. Taviot-Gueho, Y. Israeli, F. Leroux, P. Munsch, J. P. Itie, V. Briois, N. Morel-Desrosiers and J. P. Besse, *J. Phys. Chem. B*, 2003, **107**, 9243–9248.

12 F. Z. Zhang, J. L. Chen, P. Chen, Z. Y. Sun and S. L. Xu, *AIChE J.*, 2012, **58**, 1853–1861.

13 (*a*) C. Zhao, Y. Z. Yu, A. Jentys and J. A. Lercher, *Appl. Catal., B*, 2013, **132**, 282–292; (*b*) B. Mile, D. Stirling, M. A. Zammitt, A. Lovell and M. Webb, *J. Catal.*, 1988, **114**, 217–229.

14 Z. L. Yuan, L. N. Wang, J. H. Wang, S. X. Xia, P. Chen, Z. Y. Hou and X. M. Zheng, *Appl. Catal., B*, 2011, **101**, 431–440.

15 (*a*) Y. Lee and S. Oyama, *J. Catal.*, 2006, **239**, 376–389; (*b*) S. Derrouiche and D. Bianchi, *Appl. Catal., A*, 2006, **313**, 208–217.

16 (*a*) J. H. Kwak, L. Kovarik and J. Szanyi, *ACS Catal.*, 2013, **3**, 2094–2100; (*b*) G. D. Lee, M. J. Moon, J. H. Park, S. S. Park and S. S. Hong, *Korean J. Chem. Eng.*, 2005, **22**, 541–546; (*c*) N. Perkas, G. Amirian, Z. Y. Zhong, J. Teo, Y. Gofer and A. Gedanken, *Catal. Lett.*, 2009, **130**, 455–462.

17 (*a*) P. C. Zonetti, S. Letichevsky, A. B. Gaspar, E. F. Sousa-Aguia and L. G. Appel, *Appl. Catal., A*, 2014, **475**, 48–54; (*b*) H. C. Wu, Y. C. Chang, J. H. Wu, J. H. Lin, I. K. Linc and C. S. Chen, *Catal. Sci. Technol.*, 2015, **5**, 4154–4163.

18 (*a*) A. Yamaguchi and E. Iglesia, *J. Catal.*, 2010, **274**, 52–63; (*b*) J. Bradford and M. A. Vannice, *J. Catal.*, 1999, **183**, 69–75.

19 (*a*) E. A. Colbourn and W. C. Mackrodt, *Surf. Sci.*, 1982, **117**, 571–580; (*b*) S. P. Karna, R. D. Pugh, W. M. Shedd and B. K. Singaraju, *J. Non-Cryst. Solids*, 1999, **254**, 66–73; (*c*) F. Ahmed, M. K. Alam, A. Suzuki, M. Koyama, H. Tsuboi, N. Hatakeyama, A. Endou, H. Takaba, C. A. Del Carpio, M. Kubo and A. Miyamoto, *J. Phys. Chem. C*, 2009, **113**, 15676–15683.